EES Solar

ROYAL SOCIETY OF CHEMISTRY

PAPER

View Article Online
View Journal

Cite this: DOI: 10.1039/d6el00012f

Controlling crystallization dynamics of Sn–Pb mixed perovskite films for efficient scalable photovoltaics

Ting Pan,[a] Tonghan Zhao,[b] Roja Singh,[ab] Felix Laufer,[ab] Weimu Xu,[a] Julian Petermann,[ab] Benjamin Hacene,[a] Alexander Diercks,[a] Thomas Feeney,[ab] Sachin Kinge,[c] Lingyi Fang,[ab] Hang Hu *[ab] and Ulrich Wilhelm Paetzold *[ab]

A critical bottleneck for the upscaling of all-perovskite tandem solar cells is the scalable fabrication of Sn–Pb mixed narrow-bandgap (NBG) perovskite films. In response, this work researches routes to control the crystallization of blade-coated NBG perovskite thin films. Methylammonium chloride (MACl) is introduced as an additive to refine crystallization and optimize perovskite morphology during the vacuum-assisted growth (VAG) as well as the subsequent annealing step. Using *in situ* photoluminescence analysis, it is shown that MACl enhances the competition of crystal growth during the VAG and retards secondary crystallization during annealing. As a result, grain size, homogeneity, and crystallinity of blade-coated NBG perovskite films are significantly improved, leading to improved reproducibility and device performance. Champion power conversion efficiencies of 20.5% and 19.1% are demonstrated in devices with spin-coated and blade-coated perovskite absorber layers, respectively. In combination with a wide-bandgap (WBG) sub-cell fabricated using the same anti-solvent-free VAG method, a champion all-perovskite tandem solar cell realizes a power conversion efficiency (PCE) of 27.5%. These improvements are attributed to the reduced charge transport losses and enhanced charge extraction in the optimized NBG perovskite absorber. Thereby, this study enables scalable production of high-performance all-perovskite tandem photovoltaics.

Received 28th January 2026
Accepted 29th January 2026

DOI: 10.1039/d6el00012f

rsc.li/EESSolar

Broader context

All-perovskite tandem solar cells hold great promise as next-generation sustainable photovoltaic technologies due to their PCEs. However, upscaling of these tandem devices is currently hindered by challenges in scalability and reproducibility during the large-area deposition of solution-based Sn–Pb mixed NBG perovskite thin films. The characteristic rapid crystallization of NBG perovskite thin films poses a significant challenge to achieving a controllable process. Furthermore, the fundamental crystallization dynamics and evolution in the scalable fabrication of NBG perovskite films have rarely been studied. This work presents efficient *in situ* probing techniques to elucidate the crystallization dynamics of Pb–Sn mixed perovskites during scalable fabrication. The role of MACl as an additive is investigated to refine crystallization and optimize perovskite morphology. We achieve minimized efficiency losses and enhanced reproducibility in fully scalable NBG perovskite devices. By implementing the VAG method for both NBG and WBG perovskite sub-cells, we realize a PCE of 27.5% for anti-solvent-free all-perovskite tandem solar cells.

Introduction

Monolithic all-perovskite tandem photovoltaics (PVs) offer a promising and attractive approach to enhance power conversion efficiencies (PCEs) beyond the detailed balance limit of single-junction devices by stacking complementary perovskite thin film solar cells (PSCs) with narrow-bandgap (NBG) and wide-bandgap (WBG) perovskites. This PV technology offers the benefits of low-cost production and high-throughput manufacturing through solution processing, bearing the capabilities for large-scale production *via* using low-temperature and scalable processing methods to extend the possibilities of various applications.[1] Although the certified PCEs of all-perovskite tandem solar cells (APTSCs) have surpassed 30% for laboratory-scale devices,[2] larger-scale applications like all-perovskite tandem solar mini-modules still lag behind, with a reported certified PCE of 24.5%.[3] To bridge the efficiency gap, scalable fabrication of efficient NBG PSCs is highly desirable for large-area tandem manufacturing. However, boosting PCEs for scalable devices is challenging due

---

[a] *Light Technology Institute (LTI), Karlsruhe Institute of Technology (KIT), Engesserstrasse 13, 76131 Karlsruhe, Germany. E-mail: hang.hu@kit.edu; ulrich.paetzold@kit.edu*

[b] *Institute of Microstructure Technology (IMT), Karlsruhe Institute of Technology (KIT), Hermann-von-Helmholtz-Platz 1, 76344 Eggenstein-Leopoldshafen, Germany*

[c] *Materials Engineering Department, R&D 2, Toyota Motor Europe, 1930 Zaventem, Belgium*

to the complexities introduced when upscaling NBG perovskite films. These challenges include (i) maintaining film homogeneity and consistent thickness during scalable coating, (ii) mitigating potential issues arising from longer drying times and lower tolerance solvent quenching processes for as-fabricated wet perovskite films, and (iii) effectively controlling and rationally manipulating perovskite crystallization dynamics on large substrates. Blade coating has been predominantly used to fabricate NBG perovskite films for the upscaling of all-perovskite tandem photovoltaics.[3–7] To date, the most efficient laboratory-scale blade-coated NBG devices (active area <0.1 cm^2) have been achieved using anti-solvent-free quenching approaches. These include gas-quenching, which utilizes continuous gas flow during the blade-coating process (achieving PCEs from 19.0–21.4%) and vacuum-assisted growth (VAG), a vacuum-quenching step following the blade-coating process (achieving PCEs from 17.5–20.2%).[1,3,4,6–12] There remains a significant efficiency gap between the well-established spin-coating process using the anti-solvent-quenching method (champion PCE of 24.0%) and the anti-solvent-free blade-coating process (champion PCE of 21.4%).[4,13–16] This indicates that scalable coating of NBG perovskite films is the primary bottleneck for upscaling NBG PSCs and all-perovskite PVs. Therefore, a better understanding of anti-solvent-free methods, such as the seldom-studied VAG process, is imperative for control of crystallization dynamics and film-formation evolution.

The rapid crystallization of Sn-based perovskites is the key challenge in film fabrication, which is particularly uncontrollable for scalable processing methods, resulting in low-quality thin films (with poor homogeneity, increased defects, and low crystallinity). The fast and uncontrollable crystallization behavior of Pb–Sn mixed perovskite originates from the higher Lewis acidity of Sn^{2+} and the lower solubility of SnI_2 in typical solvents (*N*,*N*-dimethylformamide (DMF)/dimethyl sulfoxide (DMSO)), leaving a narrow processing window in stringent crystallization conditions.[17–19] Since a thick layer of Pb–Sn perovskite film (*e.g.*, >1 μm) is required in all-perovskite tandem PVs to achieve >90% of absorption in the near-infrared region,[20] the issue is further exacerbated by the fact that the blade-coated thick absorbers inevitably increase the risk of high roughness, poor crystallinity, increased internal stress, more solvent residue, and enhanced inhomogeneity.[5]

Formation of NBG perovskite thin films generally proceeds through two distinct stages: nucleation and crystal growth. According to the classic LaMer's mechanism, with ongoing solvent evaporation, the solution concentration reaches a critical supersaturation level, triggering spontaneous nucleation and subsequent crystal growth.[21,22] Afterwards, the solution concentration begins to decline due to the competition between solvent evaporation and solute consumption during nucleation and crystal growth.[23] Once it falls below the critical concentration, nucleation ceases, while crystal growth continues until below the saturation concentration. In brief, the rate and degree of supersaturation need to be manipulated to regulate the competition and evolution between nucleation and crystal growth through varying solvent extraction or precursor formulation.[17,24] Furthermore, a contradiction of crystal growth exists in this competition: an aggressive nucleation typically leads to the formation of smaller grain size, while a dominant crystal growth promotes larger grains but could also potentially result in void formation.[19,25] Therefore, controlling solvent quenching and annealing steps in scalable fabrication critically impacts the nucleation and crystal growth.[26] Although the crystallization kinetics of the anti-solvent quenching method are well-studied, these fundamental crystallization dynamics are not transferable to the VAG processes.[27–30] The fact is that the relatively mild attainment of supersaturation in the VAG process undergoes a larger window which necessitates stringent crystallization conditions.[23,26] The detailed crystallization dynamics and evolution in the scalable fabrication of NBG perovskite films remains unexplored, and efficient *in situ* probing techniques are lacking. Therefore, tracking and elucidating the crystallization dynamics of Pb–Sn mixed perovskites during the VAG and subsequent annealing processes is central to our work.

In this work, we focus on the crystallization dynamics of Pb–Sn mixed NBG perovskite films during VAG and the subsequent annealing processes. We utilize *in situ* and quasi-in-situ characterization techniques, particularly *in situ* photoluminescence (PL), to gain a better understanding of the dynamic evolution of perovskite formation.[22,27,31] Methylammonium chloride (MACl), which is widely used in pure Pb-based perovskites[32] but seldom studied in NBG perovskites, is introduced to improve NBG perovskite film quality and morphology in both spin-coated (SC) and blade-coated (BC) processes, and its effect on crystallization is systematically studied. Using the optimized anti-solvent-free VAG process, we achieve PCEs of 20.5% for spin-coated PSCs and 19.1% for fully scalable PSCs. By incorporating a WBG sub-cell fabricated using the VAG method, we realize a champion PCE of 27.5% for APTSCs.

Results and discussion

In Situ characterization and control of crystallization dynamics

We start with probing the crystallization dynamics for the deposition of Pb–Sn mixed NBG perovskite films by *in situ* characterizations. Pb–Sn mixed NBG perovskite films are fabricated using an established VAG method, which includes vacuum-quenching and annealing steps as illustrated in Fig. 1a. This method has been detailed in our previous work.[5,33] Given that the as-fabricated wet film forms rapidly within a few seconds at room temperature, we posit that the vacuum-quenching and annealing steps play critical roles in governing crystallization dynamics and determining the final film quality. To better understand these processes, we develop an *in situ* PL system to track and deconstruct the crystallization dynamics of Pb–Sn mixed perovskites during vacuum-quenching and annealing steps (Fig. 1a). The as-fabricated wet film is immediately transferred into a vacuum chamber connected to a rough pump and equipped with an in-house *in situ* PL characterization setup. Once the vacuum valve is opened, the *in situ* PL system simultaneously starts recording signals (*i.e.*, vacuum time of 0 s). At this moment, the chamber pressure rapidly drops (Fig. S1), and once the solution reaches the critical supersaturation level due to solvent extraction,

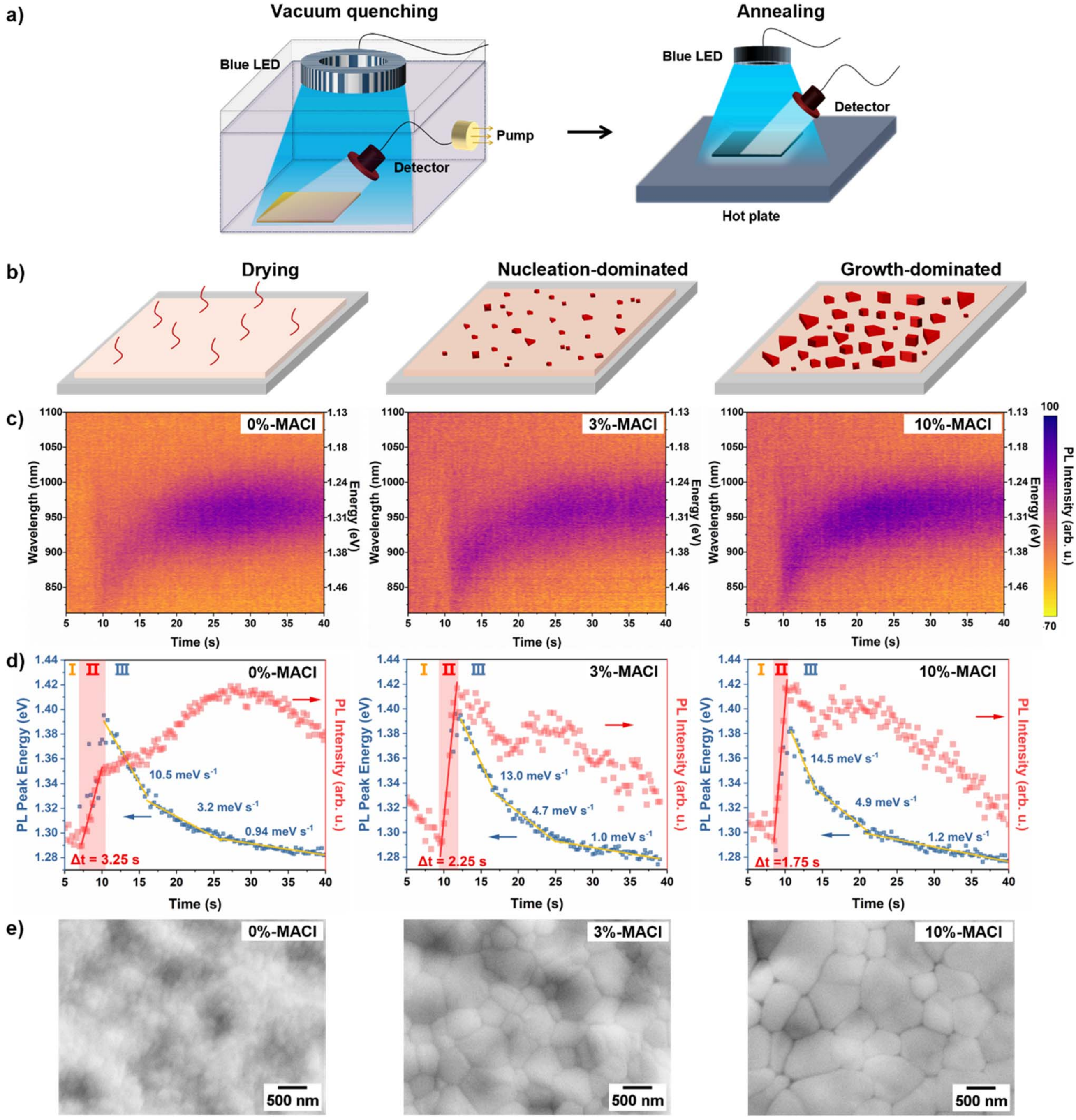

Fig. 1 (a) Schematic illustration of the *in situ* photoluminescence (PL) characterizations for the fabrication of NBG perovskite films during the vacuum-quenching and sequential annealing steps. (b) Schematic illustration of perovskite crystallization in vacuum-quenching step: drying, nucleation-dominated, and growth-dominated stages. (c) Heatmap of time-dependent *in situ* PL spectra and (d) extracted PL position and intensity of spin-coated (SC) NBG perovskite films with varied MACl concentrations during the vacuum-quenching step. Δ*t* represents the time scale of the nucleation-dominated stage. (e) Scanning electron microscopic (SEM) images of the as-fabricated SC NBG perovskite films after vacuum-quenching step (vacuum time of 20 s).

crystallization occurs. This information is reflected in the captured *in situ* PL signals. Additional, *in situ* PL data on secondary crystallization (*i.e.*, secondary crystal growth stage) is collected during the annealing step (Fig. 1a). MACl has been widely used in previous studies as an additive in pure-Pb-based perovskites to modulate crystallization and improve film quality in large-area scalable fabrication.[34] In this work, we introduce MACl as an additive (with varied concentrations of 0%, 3%, and 10%) into the Pb–Sn mixed perovskite precursor and investigate its effect on crystallization dynamics.

First, we focus on the crystallization dynamics during the vacuum-quenching step. Generally, this step involves drying, nucleation, and crystal growth processes. Although nucleation precedes crystal growth, the two processes are not strictly independent but occur simultaneously in dynamic competition.[31] Therefore, we categorize the evolution in our vacuum-quenching process into three stages: drying (stage I), nucleation-dominated (stage II), and growth-dominated (stage III) (see Fig. 1b). We collect data on these stages through the evolution of the PL spectra (Fig. 1c) and the extracted evolution of PL peak position (determined from a Pseudo-Voigt fit of the individual PL spectra) and intensity (Fig. 1d). The details of each stage are discussed below.

Stage I: this initial stage is characterized by extremely low intensity (with prominent background intensity) detectable in the range of 800 to 1100 nm (Fig. 1d) for all perovskite films (0%, 3%, and 10% MACl). We attribute this to the drying stage, as rapid solvent extraction occurs only after the pressure drops to a relatively low value. The pressure variation inside the chamber is shown in Fig. S1, where it decreases to approximately the vapor pressure of DMF (∼5.6 mbar) and DMSO (∼0.8 mbar) at around 6 seconds and 8 seconds, respectively.

Stage II: rapid solvent extraction drives the wet film into a highly supersaturated state, enabling it to overcome the energy barrier and initiate robust nucleation. The abrupt rise in the PL signal indicates the onset of nucleation, particularly as the newly emerged PL signal exhibits a broad asymmetric peak.[31,35,36] These broad features are attributed to a non-uniform distribution of nuclei, resulting in the formation of extremely small clusters due to continuous nucleation. The scattered distribution of the fitted PL peak at shorter wavelengths arises from quantum confinement, where the exciton wavefunction is confined within a smaller volume, causing the emerged nuclei to emit at higher photon energies.[24]

As the PL intensity of the 0% MACl sample approaches a temporary plateau, the 3% and 10% MACl samples reach their maximum values. We attribute the rapid increase in PL intensity to the nucleation-dominated phase. The duration of this stage is evaluated through linear fitting of PL intensity. Notably, the perovskite film with MACl additive experiences a shorter duration (Δt = 2.25 s and 1.75 s for 3% and 10% MACl, respectively) in the nucleation-dominated stage compared to the film without MACl (Δt = 3.25 s). This suggests that the MACl additive enhances the competitiveness of crystal growth over nucleation, enabling a faster transition to the growth-dominated stage. The increase in the rate of PL intensity growth (3991, 5382, and 7682 for 0%, 3%, and 10% MACl, respectively) for films with the MACl additive further supports the enhanced crystal growth competition.

Stage III: the crystallization evolves into a growth-dominated stage as the energy position undergoes a continued redshift, lasting up to ∼40 s for all perovskite films (Fig. 1d).[6,12,14] We observe a more rapid growth period, represented by the first linear fitting of PL energy in Fig. 1d for the perovskite films with MACl additive compared to those without the additive, as the redshift rate is higher for both 3% and 10% MACl (10.5, 13.0, and 14.5 meV s^{-1} for 0%, 3%, and 10% MACl, respectively). This demonstrates that the existing nanocrystals formed in stage II expand, indicating accelerated crystal growth in the first few seconds of this stage. Subsequently, the redshift slows down (3.2–4.9 meV s^{-1}) and eventually stabilizes (∼1 meV s^{-1}), which can be attributed to the reduced precursor concentration below the critical supersaturation level in the wet film.[31] The final PL peak energy of 1.28 eV reveals the distinct formation of NBG perovskite. In this stage, we propose that the MACl additive enables an accelerated competition subsequent to stage II, as the redshift rate is always higher for the film using the MACl additive compared to that without the additive (Fig. 1d).

In brief, the introduction of the MACl additive enhances the competition of crystal growth during the quenching step, enabling a faster transition from stage II to stage III and accelerating growth in stage III. The improved growth of perovskite nanocrystals results in larger crystallites and, consequently, an increased grain size. We observe that the MACl additive improves the grain size of the perovskite film before annealing, as verified by scanning electron microscopy (SEM) images (Fig. 1e), where the films are fabricated with a vacuum-quenching duration of 20 s.

Having studied the crystallization dynamics in the vacuum-quenching step, we next study the annealing step at 100 °C. The secondary crystallization during the annealing process is probed by the same *in situ* PL setup (Fig. 1a). As shown in Fig. 2a and b, the PL intensity of the 0% MACl perovskite thin film is quenched for elevated temperature and simultaneously it experiences a significant blue and subsequent redshift with a rate of 6.7 meV s^{-1} in energy. Perovskite films added with MACl show similar evolution but a retarded redshift (2.2 and 0.68 meV s^{-1} for 3% and 10% MACl, respectively). It should be noted that an adequate vacuum-quenching process induces solidification at the top surface of the perovskite film, trapping a significant amount of solvents—particularly high-boiling-point species such as DMSO—at the buried interface.[34] Upon annealing, a distinct removal of residual solvents from the perovskite films is observed during the initial few seconds of annealing (Fig. S2). These solvents migrate toward the top surface, where they can dissolve initially formed smaller crystallites and penetrate the grain boundary, thereby promoting grain fusion.[37] Subsequently, the solvents evaporate from the surface, enabling continued crystal growth and grain coalescence. The initial blueshift is likely associated with solvent migration within the film and thermal lattice expansion, whereas the subsequent redshift can be attributed to crystal growth and grain boundary formation during solvent evaporation.[38–40] The pronounced retardation of the redshift observed in MACl-containing perovskite films suggests that the MACl additive significantly slows secondary crystal growth during annealing, thereby extending the window for grain fusion.

To verify the retardation effect of MACl on the secondary crystallization, we examine the evolution of film morphology before and after annealing. Perovskite films with the MACl additive exhibit a minimum change in grain size compared to that without MACl upon annealing for 2 s (Fig. 1e and 2c). This reveals that additional MACl generates sufficient large grains in the previous quenching step (Fig. 1d) that are beneficial to the secondary growth for a longer annealing time. Specifically, the average grain size of the 3% film expands from 433 nm to 441 nm within 2 s and continues to grow up to 614 nm after 7 min (Fig. 2d and S3). In contrast, the average grain size of the 0% film grows from 167 nm to 230 nm within 2 s and further

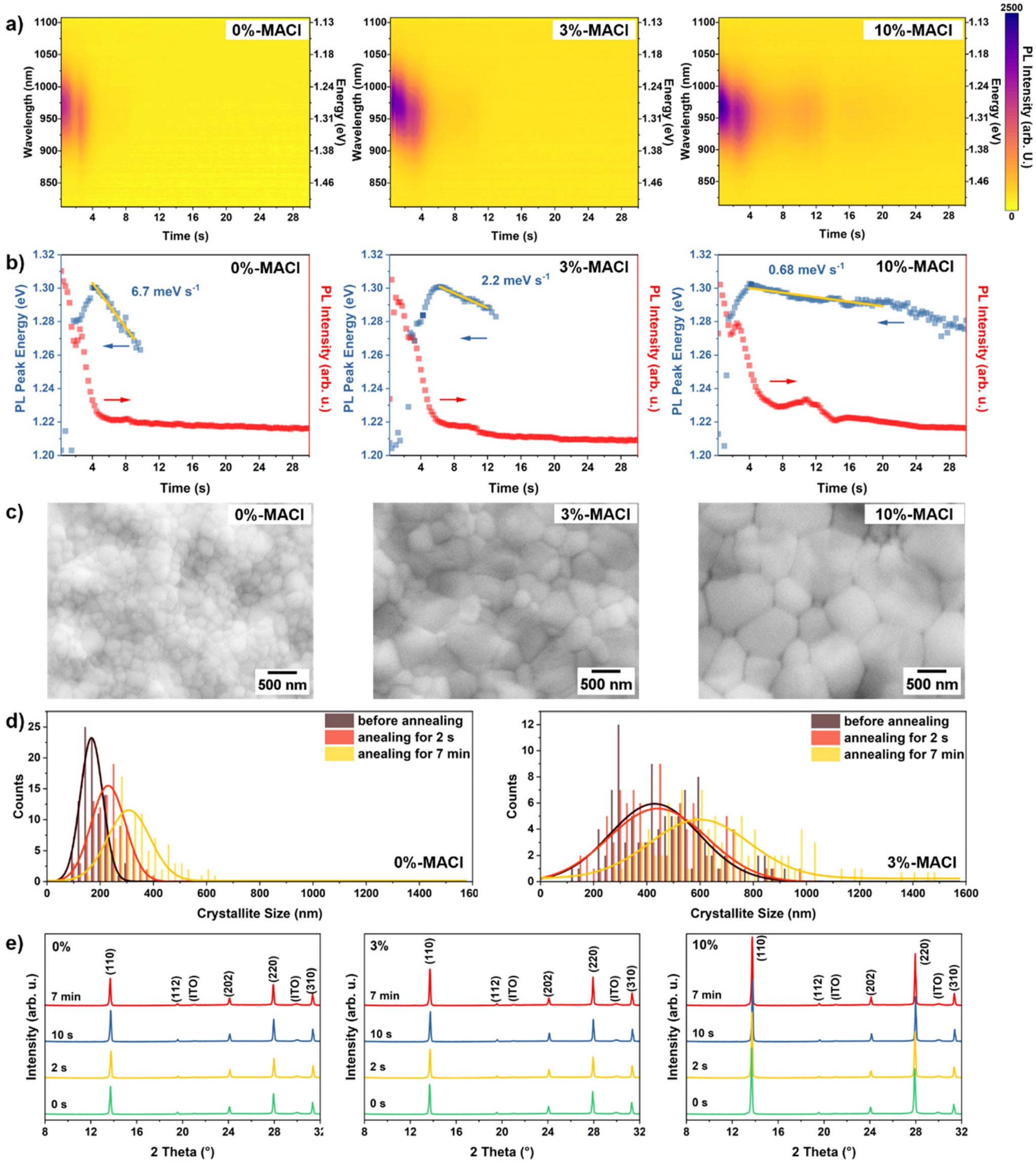

Fig. 2 (a) Time-dependent *in situ* PL spectra and (b) extracted PL position and intensity of the SC NBG perovskite films with varying MACl concentrations during the annealing step. (c) SEM images of the SC perovskite films after 2 s of annealing. (d) Grain size distribution and variation of the SC perovskite films with 0% and 3% MACl additive before annealing (0 s), and after 2 s and 7 min of annealing. (e) X-ray diffraction (XRD) patterns of the SC perovskite films with varying MACl concentrations before annealing (0 s), and after 2 s, 10 s, and 7 min of annealing.

increases to 309 nm after 7 min. These evaluations further demonstrate that MACl slows down the secondary growth (Fig. 2b), which is conducive to forming larger grain sizes (average >600 nm, some reaching >1000 nm, Fig. 2d). We hypothesize that the grain fusion is accompanied by crystal growth during the annealing step. As shown in Fig. S4, all perovskite films exhibit pinholes generated in the vacuum-quenching step prior to the annealing. The pinholes are associated with grain fusion during annealing and are eliminated after annealing (Fig. S5).

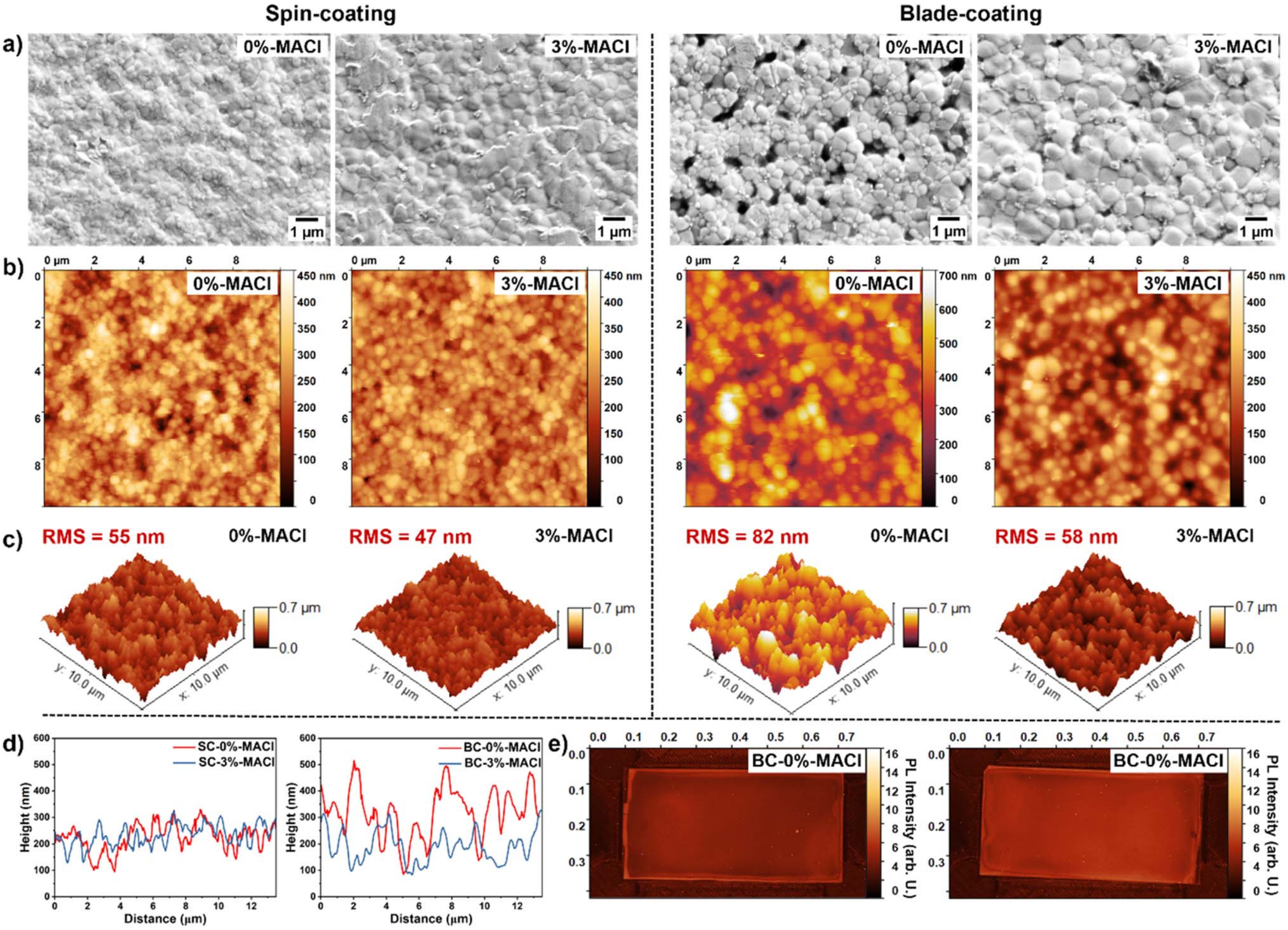

Fig. 3 (a) SEM, (b) atomic force microscopy (AFM), and (c) 3D AFM images of the NBG perovskite films with 0% and 3% of MACl additive fabricated by SC (left) and BC (right) methods, respectively. (d) Height profiles of corresponding AFM images. (e) PL mapping of blade-coated NBG perovskite films (64 × 32 mm^2) with 0% and 3% of MACl additive, respectively.

To gain insight into the influence of MACl on crystallinity evolution during annealing, X-ray diffraction (XRD, Fig. 2e) measurements are conducted before (0 s) and after annealing for 2 s, 10 s, and 7 min. With increasing annealing time, the full width at half maximum (FWHM) of the (110) diffraction peak decreases for all perovskite films (Fig. S6 and S7). Incorporating MACl enhances perovskite crystallinity, as evidenced by lower FWHM values. Furthermore, during annealing, the diffraction peak positions initially shift toward higher angles—indicating a reduction in lattice spacing—and subsequently undergo a slight regression to lower angles. This shift is negligible in the 0% MACl sample but becomes increasingly pronounced in the 3% and 10% MACl samples. Williamson–Hall analysis reveals that the initial strain increases with the introduction of the additive and progressively releases after annealing (Fig. S8 and S9).[41] No evidence of crystalline orientation changes or phase transition is observed during annealing.

Improved thin film quality in scalable processing

Having revealed the crystallization dynamics and routes to optimize thin film formation, we further examine the influence of MACl on the final film morphology for both SC and BC methods (Fig. S10). The substrate dimension for the BC process is 64 × 32 mm^2, which can be divided into 16 × 16 mm^2 substrates (the same size as the SC substrates), with each small substrate containing four cells. We use an established method employing a moderate N_2 flow to accelerate solvent extraction during vacuum-quenching for BC.[5] All SC perovskite films display dense and uniform morphology, as shown in SEM images (Fig. 3a and S11) and atomic force microscopy (AFM, Fig. 3b). As expected, the SC-3% film shows an overall increase in grain size compared to the SC-0% film, consistent with the discussion in the previous section. The SC-3% film (root mean square (RMS) = 47 nm, Fig. 3c and d) exhibits lower roughness compared to the SC-0% film (RMS = 55 nm). BC for NBG perovskites tends to produce rough, thick, and inhomogeneous films, particularly during rapid crystallization. All BC perovskite films exhibit larger grains compared to SC films (Fig. 3a and b). However, the BC-0% film displays a discontinuous surface with cavities or voids, resulting in high roughness (RMS = 82 nm). This surface feature potentially impacts charge extraction, as will be discussed later. We attribute this to the rapid, uncontrollable crystallization described in Fig. 1 and 2. Conversely, the introduction of MACl to the BC perovskite film significantly improves surface

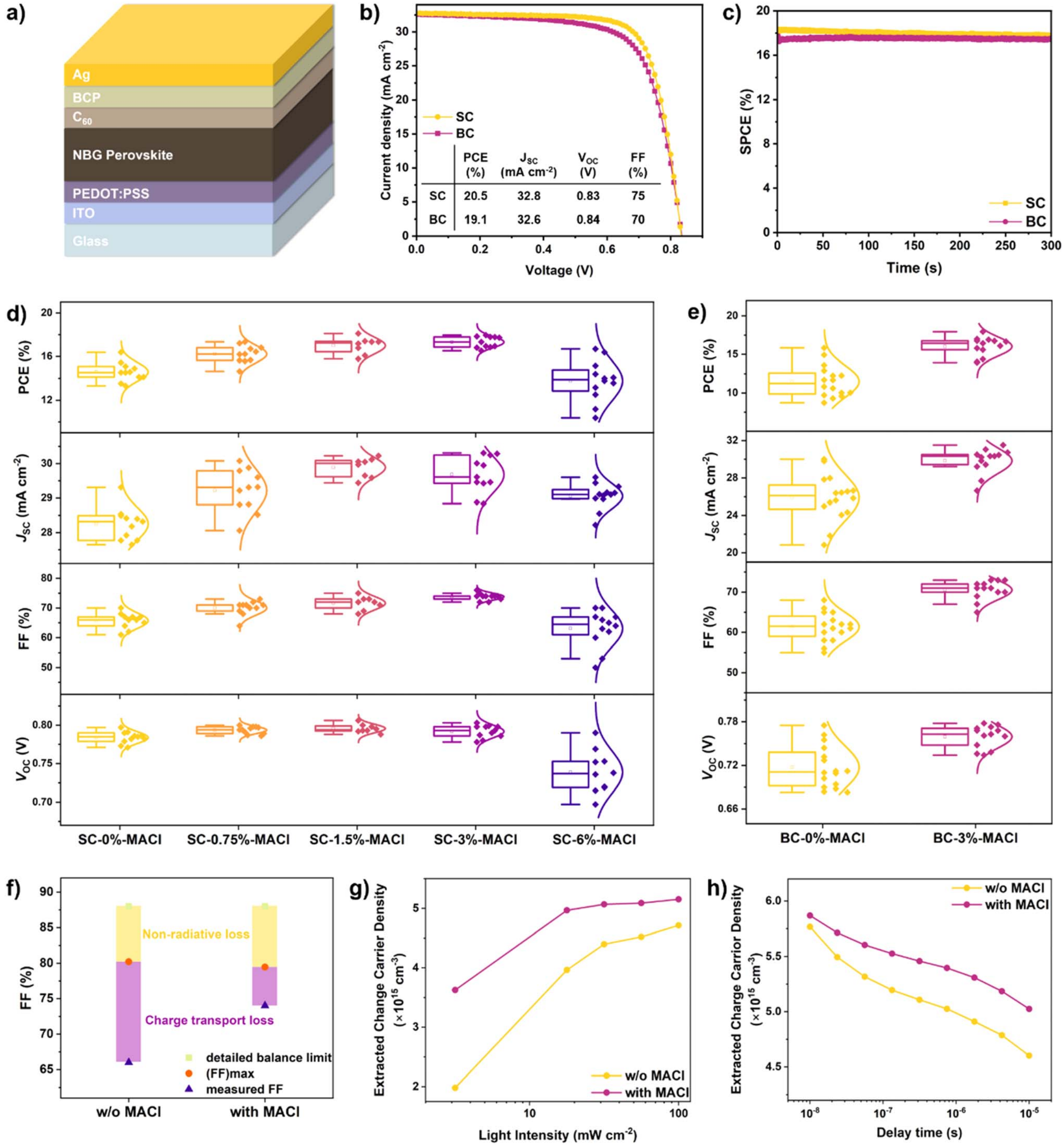

Fig. 4 (a) Schematic illustration of the architecture for NBG PSCs. (b) J–V curves of champion SC and BC NBG PSCs with an anti-reflection coating (ARC). (c) Stabilized power conversion efficiency (SPCE) of NBG PSCs under continuous AM 1.5G illumination. Statistical distribution of the photovoltaic parameters of NBG PSCs (without an ARC) with varied MACl concentrations fabricated by (d) SC and (e) BC, respectively. (f) The fill factor (FF) loss between the detailed balance limit and measured values, which mainly consists of charge transport loss and non-radiative loss. (g) Extracted charge carrier density *versus* illumination intensities (1–100 mW cm^{-2}) that was derived from charge extraction (CE) measurement for SC devices. (h) Extracted charge carrier density *versus* delay time that was derived from delay-time CE for SC devices by linearly increasing voltage (delay-time-CELIV) characterization under a constant illumination intensity of 100 mW cm^{-2}.

morphology, yielding a homogeneous, high-quality film (reduced RMS = 58 nm, Fig. 3c, **d**, and S11) with increased grain size (>1 µm, Fig. 3a) and an absence of cavities or voids (Fig. 3a and b). This enhanced homogeneity is further demonstrated by the PL mapping (Fig. 3e).

Enhanced performance and minimized charge transport loss

Encouraged by the enhanced quality of both spin-coated and blade-coated perovskite films with the introduction of MACl, we investigate its effects on device performance. For both SC and

BC fabrications, PSCs employed a p-i-n architecture consisting of glass/indium tin oxide (ITO)/poly(3,4-ethylenedioxythiophene) polystyrene sulfonate (PEDOT : PSS)/NBG perovskite/fullerene (C_{60})/bathocuproine (BCP)/Ag (Fig. 4a) with an active area of 0.105 cm^2. For fully scalable devices, the PEDOT : PSS and NBG perovskite layers are fabricated using BC, while other layers are fabricated by thermal evaporation. To elucidate the effect of MACl on PV performance, we vary the MACl concentration from 0% to 6% in SC PSCs. The best-performing devices are achieved with the addition of 3% MACl, showing significant improvements in both fill factor (FF) and short-circuit current density (J_{SC}). The champion PSC delivers a PCE of 20.5%, with a FF of 75%, open-circuit voltage (V_{OC}) of 0.83 V, and J_{SC} of 32.8 mA cm^{-2} (Fig. 4b), using an antireflection coating of MgF_2. The integrated J_{SC} derived from the external quantum efficiency (EQE; Fig. S20) spectrum reaches 31.6 mA cm^{-2}, in good agreement with the J_{SC} obtained from the *J*–*V* curve. The champion SC PSC demonstrates a stabilized PCE of 18.4% during maximum power point (MPP) tracking for 300 s under continuous AM 1.5G illumination (Fig. 4c). The device with 3% MACl exhibits comparable hysteresis (Fig. S18) but improved stability compared with the 0% MACl device, which is likely related to improved crystallization kinetics and film morphology (Fig. S19). At low MACl concentrations (<3%, Fig. 4d and S13), both J_{SC} and FF improve, while V_{OC} remains comparable, indicating a negligible effect on non-radiative recombination (Fig. S14 and S15). Therefore, we will focus on discussing the enhanced FF and J_{SC}, which originate from reduced charge transport loss and enhanced charge extraction, respectively. A higher concentration of 6% MACl leads to a significant decline across all photovoltaic parameters. A similar performance trend is observed in BC PSCs (Fig. 4e and S16). For fully scalable PSCs, we achieve a PCE of 19.1% (with a FF of 70%, a V_{OC} of 0.84 V, and a J_{SC} of 32.6 mA cm^{-2}), as well as a stabilized PCE of 17.7%. We highlight very low efficiency loss of 7% from SC (PCE = 20.5%) to fully scalable fabrication (PCE = 19.1%). It is noteworthy that the BC PSCs with MACl additive gain higher yield and better reproducibility compared to the devices without the additive (Fig. 4e), which is in line with the improved homogeneity and film quality (discussed in Fig. 3), highlighting a great potential of large-scale production for efficient modules (Fig. 3e).

To investigate the origin of the enhanced FF, we perform a FF loss analysis between the detailed balance limit and measured FF (Fig. 4f). The maximum FF (FF_{max}) can be calculated by the equations:[42,43]

$$\mathrm{FF}_{\max} = \frac{v_{\mathrm{OC}} - \ln(v_{\mathrm{OC}} + 0.72)}{v_{\mathrm{OC}} + 1}$$

$$v_{\mathrm{OC}} = \frac{qV_{\mathrm{OC}}}{n_{\mathrm{id}}k_{\mathrm{B}}T}$$

where n_{id} is the ideality factor, k_B is the Boltzmann constant, T is the absolute temperature, and q is the elementary charge. The n_{id} is determined by the illumination intensity-dependent V_{OC} (Fig. S14). In general, the FF of detailed balance limit is dominated by the non-radiative and charge transport losses, as shown in Fig. 4f. Since the non-radiative loss is comparable between the devices with and without MACl, the charge transport loss is the main factor of FF loss, which is minimized in the device with MACl. On the one hand, as already discussed above, the perovskite film fabricated with MACl produces a compact

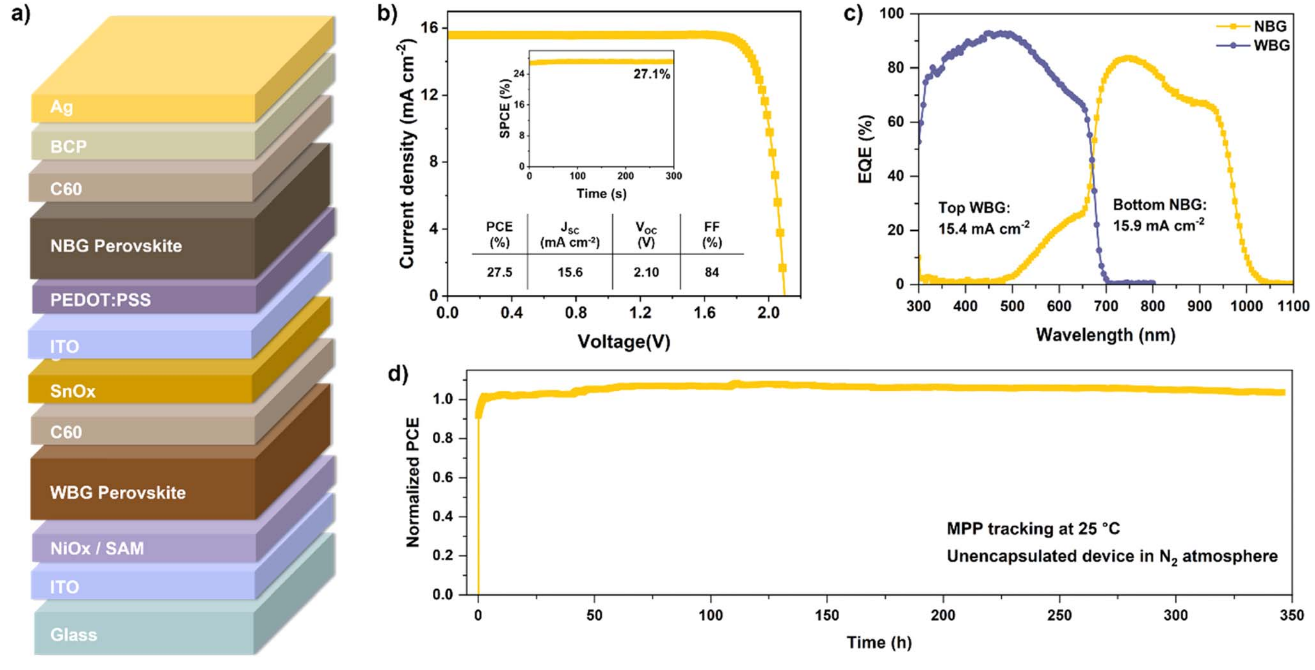

PCE (%)	J_{SC} (mA cm^{-2})	V_{OC} (V)	FF (%)
27.5	15.6	2.10	84

Fig. 5 (a) Schematic illustration of the architecture for all-perovskite tandem solar cells (APTSCs). (b) *J*–*V* curve and the SPCE of the champion APTSC under continuous AM 1.5G illumination. (c) The external quantum efficiency (EQE) curves of the APTSCs. (d) MPP tracking of a non-encapsulated APTSC under AM 1.5G illumination in N_2 atmosphere at 25 °C.

and homogeneous surface (free of cavities or voids, see Fig. 3) that facilitates the charge transport. On the other hand, the MACl additive enables the formation of a larger grain size (Fig. 2c and d), which potentially enhances the charge transport. In addition, a distinct difference in perovskite film thickness *versus* coating speed is observed between the films with and without MACl (Fig. S17). MACl additive enables the production of a thicker perovskite layer by a scalable method. The thicker perovskite absorber, potentially resulting from the improved crystal growth during vacuum-quenching and a retarded secondary crystallization during annealing, could explain the much higher J_{SC} in the MACl BC devices. Moreover, we evaluate charge carrier extraction *via* charge extraction (CE, Fig. 4g) and delay-time CE by linearly increasing voltage (delay-time-CELIV, Fig. 4h) measurements on SC samples (all perovskite films have similar thickness of 700–750 nm). The higher extracted charge carrier densities for MACl devices provide strong device-level evidence supporting the enhanced charge extraction. Overall, these results verify that MACl additive reduces charge transport loss and enhances charge extraction.

All-perovskite tandem photovoltaics *via* VAG route

We fabricated all-perovskite tandem solar cells using an optimized VAG method for both NBG and WBG sub-cells. The monolithic tandem architecture features a layer stack of glass/ITO, nickel oxide (NiO_x)/self-assembled monolayer (SAM)/WBG perovskite/passivation layers/C_{60}/atomic layer deposition (ALD)-SnO_x/ITO/PEDOT : PSS/NBG perovskite/C_{60}/BCP/Ag (Fig. 5a). The best-performing APTSC achieves a PCE of 27.5%, with a V_{OC} of 2.10 V, J_{SC} of 15.6 mA cm^{-2}, FF of 84%, and a stabilized PCE of 27.1% (Fig. 5b). The high performance of the tandem devices benefits from the optimized VAG processing of NBG and WBG sub-cells. The single junction WBG device achieve a champion PCE of 21.0% with a V_{OC} of 1.36 V, J_{SC} of 18.7 mA cm^{-2}, and FF of 83%, with negligible hysteresis (Fig. S21). The external quantum efficiency (EQE) measurement indicates integrated J_{SC} values of 15.4 mA cm^{-2} and 15.9 mA cm^{-2} for the WBG and NBG sub-cells, respectively (Fig. 5c), suggesting minimal current mismatch in the tandem architecture. We evaluate the operational stability of the non-encapsulated APTSC in the N_2-filled glovebox. The device retains initial PCE after 346 h of MPP tracking under the continuous illumination (Fig. 5d).

Conclusion

In summary, we investigate the crystallization dynamics of NBG perovskites fabricated using a VAG method during the vacuum-quenching and annealing steps using *in situ* PL measurements, combined with SEM and XRD analysis. Our results confirm that the incorporation of MACl facilitates crystal growth during the vacuum-quenching step (enhanced competition of crystal growth) and extends crystal growth during the subsequent annealing step (retarded secondary crystallization). The resulting perovskite films with MACl additive exhibit significantly larger grain sizes, improved surface uniformity, enhanced crystallinity, and increased thickness compared to films without the additive. MACl has been shown to minimize charge transport loss and enhance charge extraction. With optimized MACl concentration, we achieved PCEs of 20.5% in SC devices and 19.1% in fully scalable devices. A PCE of 27.5% is achieved for APTSCs through the implementation of an anti-solvent-free VAG method. Overall, our study provides a better understanding and guidance for further improvements in the scalable fabrication of perovskite tandem photovoltaics.

Author contributions

T. P., H. H., and U. W. P. conceived the idea and designed the experiments. T. P. did the fabrication of PSCs, most of the characterizations, and data analysis. H. H. helped with *in situ* PL and PAIOS measurements. T. Z. and A. D. performed SEM. R. S. conducted XRD. F. L. supported the vacuum-quenching system construction and PL mapping. W. X. helped with AFM measurement. J. P., B. H., and L. F. helped with the *in situ* PL system construction. T. F. and H. H. helped with ALD deposition. H. H and U. W. P. supervised the project. All authors were involved in the discussions and input of writing the manuscript.

Conflicts of interest

The authors declare no competing interests.

Data availability

The data supporting this article have been included as part of the supplementary information (SI). Supplementary information: experimental section, pressure evolution, photos of the evolution of perovskite formation, grain size distribution, SEM images, XRD patterns, strain evolution, Williamson–Hall analysis, statistical distribution of the photovoltaic parameters, illumination intensity-dependent V_{OC}, dark J–V curves, thickness variation, J–V curves, MPP tracking, and EQE. See DOI: https://doi.org/10.1039/d6el00012f.

Acknowledgements

The authors gratefully acknowledge financial support from the Helmholtz Association (project Zeitenwende, Solar Technology Acceleration Platform (Solar TAP), program-oriented funding period IV of the Helmholtz Association (Materials and Technologies for the Energy Transition, Topic 1: Photovoltaics and Wind Energy, Code: 38.01.02)), the Helmholtz Energy Materials Foundry, and the Karlsruhe School of Optics and Photonics (KSOP). T. P. acknowledges the Chinese Scholarship Council (CSC) for funding her doctoral research work.

References

1 H. Sun, K. Xiao, H. Gao, C. Duan, S. Zhao, J. Wen, Y. Wang, R. Lin, X. Zheng, H. Luo, C. Liu, P. Wu, W. Kong, Z. Liu, L. Li and H. Tan, *Adv. Mater.*, 2024, **36**, 2308706.

2 M. R. Fitzsimmons, B. Roose, Y. Han, T. Kang, Y.-H. Chiang, C.-S. Huang, Y. Lu, T. C.-J. Yang, C. Chosy, S. Guan, M. Anaya

and S. D. Stranks, *ACS Energy Lett.*, 2025, 713–725, DOI: 10.1021/acsenergylett.4c03065.

3 H. Gao, K. Xiao, R. Lin, S. Zhao, W. Wang, S. Dayneko, C. Duan, C. Ji, H. Sun, A. D. Bui, C. Liu, J. Wen, W. Kong, H. Luo, X. Zheng, Z. Liu, H. Nguyen, J. Xie, L. Li, M. I. Saidaminov and H. Tan, *Science*, 2024, **383**, 855–859.

4 K. Xiao, Y.-H. Lin, M. Zhang, R. D. J. Oliver, X. Wang, Z. Liu, X. Luo, J. Li, D. Lai, H. Luo, R. Lin, J. Xu, Y. Hou, H. J. Snaith and H. Tan, *Science*, 2022, **376**, 762–767.

5 B. Abdollahi Nejand, D. B. Ritzer, H. Hu, F. Schackmar, S. Moghadamzadeh, T. Feeney, R. Singh, F. Laufer, R. Schmager, R. Azmi, M. Kaiser, T. Abzieher, S. Gharibzadeh, E. Ahlswede, U. Lemmer, B. S. Richards and U. W. Paetzold, *Nat. Energy*, 2022, **7**, 620–630.

6 X. Dai, S. Chen, H. Jiao, L. Zhao, K. Wang, Z. Ni, Z. Yu, B. Chen, Y. Gao and J. Huang, *Nat. Energy*, 2022, **7**, 923–931.

7 C. Duan, H. Gao, K. Xiao, V. Yeddu, B. Wang, R. Lin, H. Sun, P. Wu, Y. Ahmed, A. D. Bui, X. Zheng, Y. Wang, J. Wen, Y. Wang, W. Ou, C. Liu, Y. Zhang, H. Nguyen, H. Luo, L. Li, Y. Liu, X. Luo, M. I. Saidaminov and H. Tan, *Nat. Energy*, 2025, **10**, 318–328.

8 H. Fang, W. Shen, H. Guan, G. Chen, G. Li, W. Ai, S. Fu, Z. Xu, W. Chen, P. Jia, Z. Yu, S. Wang, Z. Yu, Q. Lin, J. Wang, W. Zheng, D. Pu, G. Fang and W. Ke, *Adv. Mater.*, 2025, **37**, 2414790.

9 S. Siegrist, J. Kurisinkal Pious, H. Lai, R. K. Kothandaraman, J. Luo, V. Vlnieska, A. N. Tiwari and F. Fu, *Sol. RRL*, 2024, **8**, 2400447.

10 C. Li, Y. Pan, J. Hu, S. Qiu, C. Zhang, Y. Yang, S. Chen, X. Liu, C. J. Brabec, M. K. Nazeeruddin, Y. Mai and F. Guo, *ACS Energy Lett.*, 2020, **5**, 1386–1395.

11 X. Zhou, H. Lai, T. Huang, C. Chen, Z. Xu, Y. Yang, S. Wu, X. Xiao, L. Chen, C. J. Brabec, Y. Mai and F. Guo, *ACS Energy Lett.*, 2023, **8**, 502–512.

12 Y. Liu, H. Li, J. Wei, W. Feng, B. Tu, W. Peng, Z. Chen, L. Zeng, Y. Mai and F. Guo, *Nano Energy*, 2025, **141**, 111093.

13 A. Wang, K. Du, Z. Fang, Y. Ren, C. Zhou, Y. Yang, X. Dong, L. Li, L. Zhang, N. Yuan, G. Li, M. K. Nazeeruddin and J. Ding, *Adv. Mater.*, 2025, **37**, 2418766.

14 R. Lin, Y. Wang, Q. Lu, B. Tang, J. Li, H. Gao, Y. Gao, H. Li, C. Ding, J. Wen, P. Wu, C. Liu, S. Zhao, K. Xiao, Z. Liu, C. Ma, Y. Deng, L. Li, F. Fan and H. Tan, *Nature*, 2023, **620**, 994–1000.

15 S. Hu, K. Otsuka, R. Murdey, T. Nakamura, M. A. Truong, T. Yamada, T. Handa, K. Matsuda, K. Nakano, A. Sato, K. Marumoto, K. Tajima, Y. Kanemitsu and A. Wakamiya, *Energy Environ. Sci.*, 2022, **15**, 2096–2107.

16 H. Yuan, X. Li, W. Zhang, Y. Hu, J. Xu, T. You, Q. Weng, Y. Mao, T. Shu and J. Fang, *Adv. Mater.*, 2025, **37**, 2502680.

17 M. Yin, H. Yao, H. Qiu, C. Wu, M. Zhang and F. Hao, *Adv. Funct. Mater.*, 2024, **34**, 2404792.

18 M. Li, J. Yan, A. Zhang, X. Zhao, X. Yang, S. Yan, N. Ma, T. Ma, D. Luo, Z. Chen, L. Li, X. Li, C. Chen, H. Song and J. Tang, *Joule*, 2025, **9**, 101825.

19 X. Yang, T. Ma, H. Hu, W. Ye, X. Li, M. Li, A. Zhang, C. Ge, X. Sun, Y. Zhu, S. Yan, J. Yan, Y. Zhou, Z. a. Li, C. Chen, H. Song and J. Tang, *Nat. Photonics*, 2025, **19**, 426–433.

20 Z. Yang, Z. Yu, H. Wei, X. Xiao, Z. Ni, B. Chen, Y. Deng, S. N. Habisreutinger, X. Chen, K. Wang, J. Zhao, P. N. Rudd, J. J. Berry, M. C. Beard and J. Huang, *Nat. Commun.*, 2019, **10**, 4498.

21 M. Abbas, L. Zeng, F. Guo, M. Rauf, X.-C. Yuan and B. Cai, *Materials*, 2020, **13**, 4851.

22 T. Pan, W. Zhou, Q. Wei, Z. Peng, H. Wang, X. Jiang, Z. Zang, H. Li, D. Yu, Q. Zhou, M. Pan, W. Zhou and Z. Ning, *Adv. Mater.*, 2023, **35**, 2208522.

23 L. Zeng, S. Chen, K. Forberich, C. J. Brabec, Y. Mai and F. Guo, *Energy Environ. Sci.*, 2020, **13**, 4666–4690.

24 H. Dong, C. Ran, W. Gao, N. Sun, X. Liu, Y. Xia, Y. Chen and W. Huang, *Adv. Energy Mater.*, 2022, **12**, 2102213.

25 G. Zhang, B. Ding, Y. Ding, Y. Liu, C. Yu, L. Zeng, Y. Wang, X. Zhang, M. Liu, Q. Tian, B. Fan, Q. Liu, G. Yang, M. K. Nazeeruddin and B. Chen, *Sci. Adv.*, 2024, **10**, eadl6398.

26 S. Ternes, F. Laufer and U. W. Paetzold, *Adv. Sci.*, 2024, **11**, 2308901.

27 Y. Zhang, C. Li, H. Zhao, Z. Yu, X. Tang, J. Zhang, Z. Chen, J. Zeng, P. Zhang, L. Han and H. Chen, *Nat. Commun.*, 2024, **15**, 6887.

28 X. Liao, X. Jia, W. Li, X. Lang, J. Zhang, X. Zhao, Y. Ji, Q. Du, C.-H. Kuan, Z. Ren, W. Huang, Y. Bai, K. Zhang, C. Xiao, Q. Lin, Y.-B. Cheng and J. Tong, *Nat. Commun.*, 2025, **16**, 1164.

29 S. Zhumagali, C. Li, M. Marcinskas, P. Dally, Y. Liu, E. Ugur, C. E. Petoukhoff, M. Ghadiyali, A. Prasetio, M. Marengo, A. R. Pininti, R. Azmi, U. Schwingenschlögl, F. Laquai, V. Getautis, T. Malinauskas, E. Aydin, E. H. Sargent and S. De Wolf, *Adv. Energy Mater.*, 2025, **15**, 2404617.

30 C. Li, L. Chen, F. Jiang, Z. Song, X. Wang, A. Balvanz, E. Ugur, Y. Liu, C. Liu, A. Maxwell, H. Chen, Y. Liu, Z. Wang, P. Xia, Y. Li, S. Fu, N. Sun, C. R. Grice, X. Wu, Z. Fink, Q. Hu, L. Zeng, E. Jung, J. Wang, S. M. Park, D. Luo, C. Chen, J. Shen, Y. Han, C. A. R. Perini, J.-P. Correa-Baena, Z.-H. Lu, T. P. Russell, S. De Wolf, M. G. Kanatzidis, D. S. Ginger, B. Chen, Y. Yan and E. H. Sargent, *Nat. Energy*, 2024, **9**, 1388–1396.

31 S. Qiu, M. Majewski, L. Dong, D. Jang, V. M. L. Corre, J. G. Cerrillo, O. J. J. Ronsin, F. Yang, F. Guo, K. Zhang, L. Lüer, J. Harting, T. Du, C. J. Brabec and H.-J. Egelhaaf, *Adv. Energy Mater.*, 2024, **14**, 2303210.

32 F. Guo, S. Qiu, J. Hu, H. Wang, B. Cai, J. Li, X. Yuan, X. Liu, K. Forberich, C. J. Brabec and Y. Mai, *Advanced Science*, 2019, **6**, 1901067.

33 H. Hu, S. Moghadamzadeh, R. Azmi, Y. Li, M. Kaiser, J. C. Fischer, Q. Jin, J. Maibach, I. M. Hossain, U. W. Paetzold and B. Abdollahi Nejand, *Adv. Funct. Mater.*, 2022, **32**, 2107650.

34 H. Hu, D. B. Ritzer, A. Diercks, Y. Li, R. Singh, P. Fassl, Q. Jin, F. Schackmar, U. W. Paetzold and B. A. Nejand, *Joule*, 2023, **7**, 1574–1592.

35 P. Barua and I. Hwang, *Materials*, 2023, **16**, 2110.

36 N. Mrkyvkova, V. Held, P. Nádaždy, R. Subair, E. Majkova, M. Jergel, A. Vlk, M. Ledinsky, M. Kotlár, J. Tian and P. Siffalovic, *J. Phys. Chem. Lett.*, 2021, **12**, 10156–10162.

37 C. Ge, Q. Xu, D. Liu, W. Ye, Y. Zhu, P. Zhang, J. Yang, G. Liang, L. Xu, Y. Zhou, H. Song, C. Chen and J. Tang, *Energy Environ. Sci.*, 2025, **18**, 430–438.

38 X. Wu, S. Omagari, J. Gao and M. Vacha, *Adv. Opt. Mater.*, 2024, **12**, 2301479.

39 Y. Liang, Y. Yang, H. Xie, X. Cheng, X. Zhu, C. Yuan, Z. Wang, H. Li and K. Yang, *J. Mol. Struct.*, 2025, **1321**, 139787.

40 H. Zhang, Z. Bi, Z. Zhai, H. Gao, Y. Liu, M. Jin, M. Ye, X. Li, H. Liu, Y. Zhang, X. Li, H. Tan, Y. Xu and L. Yang, *Adv. Funct. Mater.*, 2024, **34**, 2302214.

41 D. Liu, D. Luo, A. N. Iqbal, K. W. P. Orr, T. A. S. Doherty, Z.-H. Lu, S. D. Stranks and W. Zhang, *Nat. Mater.*, 2021, **20**, 1337–1346.

42 J. Wang, J. Zhang, Y. Zhou, H. Liu, Q. Xue, X. Li, C.-C. Chueh, H.-L. Yip, Z. Zhu and A. K. Y. Jen, *Nat. Commun.*, 2020, **11**, 177.

43 Z. Li, X. Sun, X. Zheng, B. Li, D. Gao, S. Zhang, X. Wu, S. Li, J. Gong, J. M. Luther, Z. a. Li and Z. Zhu, *Science*, 2023, **382**, 284–289.